
Article:
de Borst, R. orcid.org/0000-0002-3457-3574 (2017) A classification of poromechanical interface elements. Journal of Modeling in Mechanics and Materials, 1 (1). 20160160. ISSN 2328-2355

https://doi.org/10.1515/jmmm-2016-0160

A classification of poromechanical interface elements

René de Borst[a,*]

[a] *University of Sheffield, Department of Civil and Structural Engineering, Sir Frederick Mappin Building, Mappin Street, Sheffield S1 3JD, UK*

Abstract

Interface elements are a classical approach to represent discrete cracks, joints and faults. The basic kinematic and constitutive aspects are recapitulated and the extension to hydromechanical conditions is elaborated. A classification is presented of hydromechanical interface elements, depending on the multiplicity of the pressure degree of freedom, and the physical implications of the different possibilities are explained.

Keywords: poromechanics, fracture, hygro-mechanical interfaces, finite elements

1. Introduction

Fracture in fluid-saturated porous media is a challenging, multi-scale problem with moving internal boundaries, characterised by a high degree of complexity. Moreover, fracture initiation and propagation in fluid-saturated porous materials occur frequently, indicating that there is also a large practical relevance. The existence and propagation of cracks in porous materials can be undesirable, like those that form in human tissues, or when the storage of waste in rocks or salt domes is concerned. But cracking can also be a pivotal element in an industrial process, for example hydraulic fracturing in the oil and gas industry. Another important application area is the rupture of geological faults, where the change in geometry of a fault can drastically affect local fluid flow as the faults can act as channels in which the fluid can flow freely.

Interface elements are a powerful and relatively simple manner to simulate crack initiation and propagation [1, 2]). Remeshing has been introduced to decouple the crack propagation path from the original mesh [3, 4, 5, 6, 7]. The extended finite element method [8, 9] has been proposed as an alternative approach. It decouples the crack propagation path from the underlying discretisation, and has been a main carrier of numerical approaches to fracture for more than a decade. The extension to fracture in fluid-saturated porous media has been accomplished as well [10, 11, 12, 13, 14, 15, 16].

The main subject of this paper is a classification of discretisation technologies for poroelastic interfaces, starting from the case that the pressure is continuous across the discontinuity, but where the pressure gradient is discontinuous. This relatively simple formulation already allows for the transport and storage of liquid inside the crack,

[*] Corresponding author: René de Borst
Email address: r.deborst@sheffield.ac.uk (René de Borst)

provided that the pressure gradient can be discontinuous. In the extended finite element method this is achieved by partitioning the pressures at both sides of the discontinuity by a signed distance function [11, 13]. In interface elements [17] a discontinuous pressure gradient across the discontinuity comes in naturally, as by definition they are C^0-continuous with respect to the pressure across the interface. Pressure continuity has also been assumed by Armero and Callari [18] using a discontinuous enrichment for the displacements exploiting the Enhanced Assumed Strain concept. In the latter case flow and storage inside the cracks is *not* enabled since, within the element, the continuity of the pressure field is higher than C^0.

Other poroelastic interfaces can be constructed starting from the assumption that the pressure is discontinuous orthogonal to the discontinuity [10, 12, 19, 20], or that a Dirac function is superimposed on the interpolation functions for the pressure field as in [21]. Again, it depends on the applied discretisation technology whether flow and storage are enabled inside the crack. In [10, 12] this has been achieved by partitioning the pressure field at both sides of the discontinuity through a Heaviside function placed at it, which enables the gradient to be discontinuous as well. Likewise, it is naturally embedded in interface elements with a double pressure node because of the C^{-1} continuity in the pressure field at the interface [19, 20]. It is finally noted that (pressure-continuous) poroelastic interface elements have also been developed within the context of isogeometric analysis [22], including the possibility of fluid flow and storage in the discontinuity [23].

Herein, we start with a brief recapitulation of three-dimensional, mechanical interface elements. Next, extension is made to interfaces that are embedded in a poromechical medium, and that allow for mass transport within the interface. Three formulations are distinguished, with a single pressure node, a double pressure node, and a triple pressure node at the discontinuity. The strong and weak forms are given, as well as the discretised format, and the physical implications of the different choices. Examples with single and double pressure nodes conclude the paper.

2. Standard interface elements

Interface elements are normally inserted a priori in the finite element mesh, unless remeshing is used. For stationary discontinuities, or when the direction of the propagation is known, interface elements can be used in a simple manner. When internal discontinuities propagate, they can be used in combination with remeshing.

The kinematic quantities in continuous interface elements are a set of mutually orthogonal, relative displacements: $[\![u_n]\!]$ for the opening mode, and $[\![u_s]\!], [\![u_t]\!]$ for the two sliding modes. When collecting the relative displacements in a vector

$$[\![\mathbf{u}]\!] = ([\![u_n]\!], [\![u_s]\!], [\![u_t]\!])^{\mathrm{T}}, \tag{1}$$

which is defined in a local s, n, t-coordinate system, they can be related to the displacements $\mathbf{u}^+$ at the upper side of the interface, Γ_d^+, and the displacements $\mathbf{u}^-$ at the lower side of the interface, Γ_d^-, via

$$[\![\mathbf{u}]\!] = \mathbf{R}\,(\mathbf{u}^+ - \mathbf{u}^-)\,, \tag{2}$$

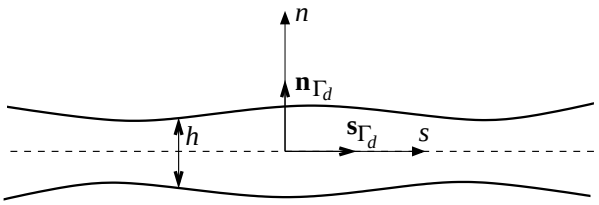

Figure 1: Geometry and local coordinate system in the interface

where $\mathbf{u}^+, \mathbf{u}^-$ are expressed in the global x, y, z-coordinate system, and $\mathbf{R} = (\mathbf{s}_{\Gamma_d}, \mathbf{n}_{\Gamma_d}, \mathbf{t}_{\Gamma_d})$ is the standard rotation matrix between the local and the global coordinate system, with $\mathbf{s}_{\Gamma_d}, \mathbf{t}_{\Gamma_d}$ mutually orthogonal unit vectors aligned with the discontinuity, and $\mathbf{n}_{\Gamma_d}$ the unit vector normal to the discontinuity, see also Figure 1 for a two-dimensional representation. The displacements are interpolated in a standard manner as:

$$\mathbf{u} = \mathbf{H}\mathbf{a}, \tag{3}$$

where

$$\mathbf{H} = \begin{bmatrix} \mathbf{h} & \mathbf{0} & \mathbf{0} \\ \mathbf{0} & \mathbf{h} & \mathbf{0} \\ \mathbf{0} & \mathbf{0} & \mathbf{h} \end{bmatrix} \tag{4}$$

and $\mathbf{a}$ is the nodal displacement array that contains the degrees of freedom related to the N nodes in case of a standard continuum element. For an interface element, however, the nodes are doubled, one set of N nodes for the Γ_d^+ side of the interface, and another set of N nodes for the Γ^- side, cf Figure 2. The $1 \times N$ matrices $\mathbf{h}$ contain the shape functions $h_1, ..., h_N$:

$$\mathbf{h} = \begin{pmatrix} h_1 \\ \cdots \\ \cdots \\ h_N \end{pmatrix}. \tag{5}$$

The relation between the nodal displacements and the relative displacements for interface elements then reads:

$$[\![\mathbf{u}]\!] = \mathbf{R}\,(\mathbf{u}^+ - \mathbf{u}^-) = \mathbf{R}\,(\mathbf{H}\mathbf{a}^+ - \mathbf{H}\mathbf{a}^-) = \mathbf{R}\mathbf{B}_d\tilde{\mathbf{a}}, \tag{6}$$

with

$$\mathbf{B}_d = \begin{bmatrix} -\mathbf{h} & +\mathbf{h} & \mathbf{0} & \mathbf{0} & \mathbf{0} & \mathbf{0} \\ \mathbf{0} & \mathbf{0} & -\mathbf{h} & +\mathbf{h} & \mathbf{0} & \mathbf{0} \\ \mathbf{0} & \mathbf{0} & \mathbf{0} & \mathbf{0} & -\mathbf{h} & +\mathbf{h} \end{bmatrix}. \tag{7}$$

the relative displacement-nodal displacement matrix for the interface element, and $\tilde{\mathbf{a}}$ containing the discrete nodal displacements at both sides of the interface expressed in the global x, y, z-coordinate system. It is noted that, although $\tilde{\mathbf{a}}$ contains twice the number of degrees of freedom as does $\mathbf{a}$ per element, no degrees of freedom are added to the system.

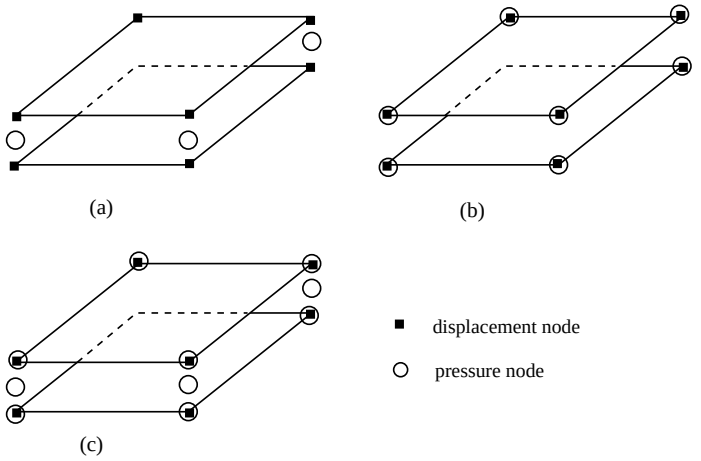

Figure 2: Interface elements enriched with pressure nodes

In the local coordinate system, the cohesive tractions $\mathbf{t}_d^{\text{loc}}$ are related to the relative displacements $[\![\mathbf{u}]\!]$ via a nonlinear relation:

$$\mathbf{t}_d^{\text{loc}} = \mathbf{t}_d^{\text{loc}}([\![\mathbf{u}]\!], \kappa), \tag{8}$$

with κ a history parameter. Similar to the relative displacements, the traction vector $\mathbf{t}_d^{\text{loc}}$ can be related to the tractions in the global coordinate system using the rotation matrix $\mathbf{R}$:

$$\mathbf{t}_d^{\text{loc}} = \mathbf{R}\mathbf{t}_d \tag{9}$$

For use in a Newton-Raphson iterative procedure this constitutive relation can be linearised as:

$$\mathrm{d}\mathbf{t}_d^{\text{loc}} = \mathbf{D}_d \, \mathrm{d}[\![\mathbf{u}]\!], \tag{10}$$

with 'd' a small increment, and

$$\mathbf{D}_d = \frac{\partial \mathbf{t}_d^{\text{loc}}}{\partial [\![\mathbf{u}]\!]}. \tag{11}$$

The limiting case that $\mathbf{t}_d^{\text{loc}} = \mathbf{0}$ obviously represents a traction-free crack.

For the purely mechanical case, the equilibrium equation reads:

$$\nabla \cdot \boldsymbol{\sigma} = \mathbf{0}. \tag{12}$$

After multiplication by a test function $\boldsymbol{\eta}$ and application of Gauss' theorem, the weak form is obtained:

$$\begin{aligned} \int_\Omega \nabla\boldsymbol{\eta} : \boldsymbol{\sigma} \mathrm{d}\Omega \\ - \int_{\Gamma_d^+} \boldsymbol{\eta}^+ \cdot (\mathbf{n}_{\Gamma_d^+} \cdot \boldsymbol{\sigma}^+) \mathrm{d}\Omega - \int_{\Gamma_d^-} \boldsymbol{\eta}^- \cdot (\mathbf{n}_{\Gamma_d^-} \cdot \boldsymbol{\sigma}^-) \mathrm{d}\Omega = \int_{\Gamma_t} \boldsymbol{\eta} \cdot \mathbf{t}_p \mathrm{d}\Omega, \end{aligned} \tag{13}$$

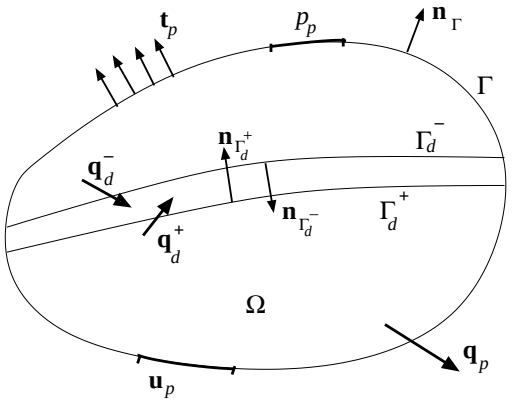

Figure 3: Body Ω with external boundary Γ and internal boundaries Γ_d^+ and Γ_d^-

with $\mathbf{t}_p$ the prescribed tractions at the external traction boundary Γ_t. Since $\Gamma_d = \Gamma_d^+ = \Gamma_d^-$, which defines the zero-thickness interface Γ_d, the surface integrals at this interface can be elaborated as follows. We define:

$$\mathbf{n}_{\Gamma_d} = \mathbf{n}_{\Gamma_d^-} = -\mathbf{n}_{\Gamma_d^+} \tag{14}$$

see also Figure 3. Next, we assume traction continuity between the interface and the bulk:

$$\boldsymbol{\sigma}^+ \cdot \mathbf{n}_{\Gamma_d^-} = -\boldsymbol{\sigma}^- \cdot \mathbf{n}_{\Gamma_d^+} = \mathbf{t}_d, \tag{15}$$

with $\mathbf{t}_d$ the cohesive tractions. Using Equation (15), the equilibrium equation, Equation (13), can be reworked as:

$$\int_\Omega \nabla\boldsymbol{\eta} : \boldsymbol{\sigma} \mathrm{d}\Omega + \int_{\Gamma_d} [\![\boldsymbol{\eta}]\!] \cdot \mathbf{t}_d^{\mathrm{loc}} \mathrm{d}\Gamma = \int_{\Gamma_t} \boldsymbol{\eta} \cdot \mathbf{t}_p \mathrm{d}\Gamma, \tag{16}$$

We discretise the test function $\boldsymbol{\eta}$ in a Bubnov-Galerkin sense:

$$\boldsymbol{\eta} = \mathbf{H}\mathbf{w} \tag{17}$$

with $\mathbf{w}$ a nodal array. Noting that

$$[\![\boldsymbol{\eta}]\!] = \mathbf{R}\mathbf{B}_d\tilde{\mathbf{w}} \tag{18}$$

cf. Equation (6), and following standard procedures the discrete form of Equation (16) results:

$$\int_\Omega \mathbf{w}^{\mathrm{T}}\mathbf{B}_u^{\mathrm{T}}\boldsymbol{\sigma} \mathrm{d}\Omega + \int_{\Gamma_d} \tilde{\mathbf{w}}^{\mathrm{T}}\mathbf{B}_d^{\mathrm{T}} \underbrace{\mathbf{R}^{\mathrm{T}}\mathbf{t}_d^{\mathrm{loc}}}_{\mathbf{t}_d} \mathrm{d}\Gamma = \int_{\Gamma_t} \mathbf{w}^{\mathrm{T}}\mathbf{B}_u^{\mathrm{T}}\mathbf{t}_p \mathrm{d}\Gamma, \tag{19}$$

with

$$\mathbf{B}_u = \mathbf{L}\mathbf{H}, \tag{20}$$

$$\mathbf{L} = \begin{bmatrix} \frac{\partial}{\partial x} & 0 & 0 \\ 0 & \frac{\partial}{\partial y} & 0 \\ 0 & 0 & \frac{\partial}{\partial z} \\ \frac{\partial}{\partial y} & \frac{\partial}{\partial x} & 0 \\ 0 & \frac{\partial}{\partial z} & \frac{\partial}{\partial y} \\ \frac{\partial}{\partial z} & 0 & \frac{\partial}{\partial x} \end{bmatrix} \tag{21}$$

the matrix that relates the strains, $\boldsymbol{\epsilon}$, to the displacements a continuum element: $\boldsymbol{\epsilon} = \mathbf{Lu}$. Considering that this identity must hold for all admissible test functions, and rearranging yields:

$$\mathbf{f}^{\text{ext}} - \mathbf{f}^{\text{int}} = \mathbf{0}. \tag{22}$$

with the external force vector

$$\mathbf{f}^{\text{ext}} = \int_{\Gamma_t} \mathbf{B}_u^{\mathrm{T}} \mathbf{t}_p \mathrm{d}\Gamma \tag{23}$$

and the internal force vector

$$\mathbf{f}^{\text{int}} = \int_{\Omega} \mathbf{B}_u^{\mathrm{T}} \boldsymbol{\sigma} \mathrm{d}\Omega + \int_{\Gamma_d} \mathbf{B}_d^{\mathrm{T}} \mathbf{t}_d \mathrm{d}\Gamma. \tag{24}$$

The set of Equations (22) is generally nonlinear and is typically solved using a Newton-Raphson scheme for every time step. Defining the material tangential stiffness matrix

$$\mathbf{D}_{j-1} = \left. \frac{\partial \boldsymbol{\sigma}}{\partial \boldsymbol{\epsilon}} \right|_{j-1}, \tag{25}$$

which sets the relation between the change in the stress $\mathrm{d}\boldsymbol{\sigma}$ and that in the strain, $\mathrm{d}\boldsymbol{\epsilon}$, from iteration $j-1$ to iteration j in the continuum, cf. [24]:

$$\mathrm{d}\boldsymbol{\sigma} = \mathbf{D}_{j-1}\, \mathrm{d}\boldsymbol{\epsilon}, \tag{26}$$

and utilising the material tangential stiffness matrix for the interface, $\mathbf{D}_d$, the tangential stiffness matrix after iteration $j-1$, can be derived as:

$$\mathbf{K}_{j-1} = \frac{\partial \mathbf{f}_{j-1}^{int}}{\partial \mathbf{a}} = \underbrace{\int_{\Omega} \mathbf{B}_u^{\mathrm{T}} \mathbf{D}_{j-1} \mathbf{B}_u \mathrm{d}\Gamma}_{\mathbf{K}_{j-1}^{\Omega}} + \underbrace{\int_{\Gamma_d} \mathbf{B}_d^{\mathrm{T}} \mathbf{R}^{\mathrm{T}} \mathbf{D}_{d,j-1} \mathbf{R} \mathbf{B}_d \mathrm{d}\Gamma}_{\mathbf{K}_{j-1}^{\Gamma_d}}. \tag{27}$$

The iterative improvement $\mathrm{d}\mathbf{a}$ of the nodal displacements in iteration j then follows from:

$$\mathbf{K}_{j-1} \mathrm{d}\mathbf{a} = \mathbf{f}^{\text{ext}} - \mathbf{f}_{j-1}^{\text{int}}. \tag{28}$$

Interface elements are often inserted in the finite element mesh prior to the computation, and a finite stiffness must be assigned in the pre-cracking phase with at least the diagonal elements being non-zero. Prior to crack initiation, the stiffness matrix in the interface element reads:

$$\mathbf{D}_d = \begin{bmatrix} d_n & 0 & 0 \\ 0 & d_s & 0 \\ 0 & 0 & d_t \end{bmatrix},$$

with d_n a high (dummy) stiffness normal to the interface and d_s and d_t the tangential stiffnesses. It is noted that in the pre-cracking phase the numerical integration of interface elements can entail inaccuracies [2].

3. Poromechanical interface elements

For a poromechanical interface element, each node is augmented with one or more pressure degrees of freedom. For a single pressure degree of freedom, the pressure is continuous at the internal discontinuity [11, 13, 17, 23]. When two pressure degrees of freedom are added, the pressure can be discontinuous across the internal boundary Γ_d [10, 12, 19, 20]. Alternatively, one can assume that the same pressure exists at both sides of the discontinuity, but that this pressure is different from that inside the discontinuity [21]. This model, in which a regularised Dirac function is superimposed on the regular pressure field, also requires two degrees of freedom at the internal boundary. However, from a physical point of view the case that the pressure is the same at both sides of the interface may be less relevant, and its treatment is not pursued here. The most general case is when the pressures at both sides of the crack are allowed to differ, and can be different from the fluid pressure within the crack as well, a model with three pressure nodes ensues [26]. It is finally noted that all three options result in a pressure gradient which can be discontinuous, allowing for storage and fluid flow within the discontinuity. Indeed, the pressure across the interface element is at most interpolated with a C^0-continuity, yielding a pressure gradient that is at most C^{-1}-continuous.

In a fluid-saturated porous medium, the total stress is composed of a solid and a fluid part:

$$\boldsymbol{\sigma} = \boldsymbol{\sigma}_s + \boldsymbol{\sigma}_f \tag{29}$$

Using the Biot coefficient α, which takes into account the compressibility of the solid grains [27], the total stress can be written as:

$$\boldsymbol{\sigma} = \boldsymbol{\sigma}_s - \alpha p \mathbf{I} \tag{30}$$

with p the (apparent) fluid pressure and $\mathbf{I}$ the unit tensor. In a similar spirit we have

$$\boldsymbol{\sigma}^+ \cdot \mathbf{n}_{\Gamma_d^-} = -\boldsymbol{\sigma}^- \cdot \mathbf{n}_{\Gamma_d^+} = \mathbf{t}_d - p\mathbf{n}_{\Gamma_d} \tag{31}$$

instead of Equation (15). When inserting Equations (30) and (31) into the weak form of the equilibrium equation, Equation (13), and using Equation (14), we now obtain:

$$\int_\Omega \nabla\boldsymbol{\eta} : (\boldsymbol{\sigma}_s - \alpha p\mathbf{I})\mathrm{d}\Omega + \int_{\Gamma_d} [\![\boldsymbol{\eta}]\!] \cdot (\mathbf{t}_d^{\mathrm{loc}} - p\mathbf{n}_{\Gamma_d}^{\mathrm{loc}})\, \mathrm{d}\Gamma = \int_{\Gamma_t} \boldsymbol{\eta} \cdot \mathbf{t}_p \mathrm{d}\Gamma. \tag{32}$$

The mass balance of a fluid-saturated porous medium reads, e.g. [10, 27]:

$$\alpha\nabla \cdot \dot{\mathbf{u}}_s + n_f\,(\dot{\mathbf{u}}_f - \dot{\mathbf{u}}_s) + \frac{1}{M}\frac{\partial p}{\partial t} = 0 \tag{33}$$

with n_f the porosity and M the Biot modulus. Inserting Darcy's relation

$$n_f\,(\dot{\mathbf{u}}_f - \dot{\mathbf{u}}_s) = -k_f \nabla p \tag{34}$$

with k_f the permeability then gives:

$$\alpha \nabla \cdot \dot{\mathbf{u}}_s - \nabla \cdot \left(k_f \nabla p \right) + \frac{1}{M} \frac{\partial p}{\partial t} = 0. \tag{35}$$

To arrive at the weak form, we multiply by a test function for the pressure, ζ. Integrating over the domain Ω and using the divergence theorem and the appropriate boundary condition leads to:

$$\begin{aligned} -\int_\Omega \alpha \zeta \nabla \cdot \dot{\mathbf{u}}_s \, \mathrm{d}\Omega - \int_\Omega k_f \nabla \zeta \cdot \nabla p \, \mathrm{d}\Omega - \int_\Omega \zeta \frac{1}{M} \frac{\partial p}{\partial t} \mathrm{d}\Omega \\ - \int_{\Gamma_d^+} \zeta^+ \mathbf{n}_{\Gamma_d^+} \cdot \mathbf{q}_d^+ \mathrm{d}\Gamma - \int_{\Gamma_d^-} \zeta^- \mathbf{n}_{\Gamma_d^-} \cdot \mathbf{q}_d^- \mathrm{d}\Gamma = \int_{\Gamma_q} \zeta \mathbf{n}_\Gamma \cdot \mathbf{q}_p \mathrm{d}\Gamma, \end{aligned} \tag{36}$$

with $\mathbf{q}_p$ the prescribed flux on the flux boundary Γ_q. It is noted that the equation has been multiplied by -1 as well in order to preserve symmetry after linearisation.

Having assumed equilibrium between the cavity and the bulk, Equation (15), invoking Equation (14), and noting that the (cohesive) tractions $\mathbf{t}_d$ have a unique value, the fluid pressure p has the same value at both faces of the cavity: $p = p^+ = p^-$. Using a Bubnov-Galerkin approach, this implies that also the test function ζ attains the same value at both faces: $\zeta = \zeta^+ = \zeta^-$. With this corollary, the weak form of the mass balance is modified as:

$$\begin{aligned} -\int_\Omega \alpha \zeta \nabla \cdot \dot{\mathbf{u}}_s \, \mathrm{d}\Omega - \int_\Omega k_f \nabla \zeta \cdot \nabla p \, \mathrm{d}\Omega - \int_\Omega \zeta \frac{1}{M} \frac{\partial p}{\partial t} \mathrm{d}\Omega \\ + \int_{\Gamma_d} \zeta \mathbf{n}_{\Gamma_d} \cdot [\![\mathbf{q}_d]\!] \mathrm{d}\Gamma = \int_\Gamma \zeta \mathbf{n}_\Gamma \cdot \mathbf{q}_p \mathrm{d}\Gamma \end{aligned} \tag{37}$$

A jump in the flux,

$$[\![\mathbf{q}_d]\!] = \mathbf{q}_d^+ - \mathbf{q}_d^- \tag{38}$$

has now emerged in the integral for the discontinuity, see Figure 3. This term is multiplied by the normal $\mathbf{n}_{\Gamma_d}$ to Γ_d, resulting in a jump of the flow normal to the internal discontinuity. Accordingly, the flow can be discontinuous at Γ_d and some of the fluid that flows into the crack can be stored or be transported within the crack. The jump in the flux is therefore a measure of the net fluid exchange between a discontinuity (the cavity) and the surrounding bulk material. It is emphasised that because of the presence of a discontinuity inside the domain Ω, the power of the external tractions on Γ_d and the normal fluid flux through the faces of the discontinuity are essential features of the weak formulation. Indeed, these terms enable the momentum and mass couplings between a discontinuity – the mesoscopic scale – and the surrounding porous medium – the macroscopic scale.

3.1. Interface elements with a continuous pressure

We first consider the case of a continuous pressure across the interface element, so that there is a single pressure node only, Figure 2(a). The pressure in the interface is then interpolated as:

$$p = \mathbf{h}_p^{\mathrm{T}} \mathbf{p}, \tag{39}$$

where

$$\mathbf{h}_p^{\mathrm{T}} = \left((h_p)_1, ..., (h_p)_N\right) \tag{40}$$

contains the interpolation polynomials $(h_p)_1, ..., (h_p)_N$ for the pressure, and

$$\mathbf{p} = \begin{pmatrix} p_1 \\ ... \\ ... \\ p_N \end{pmatrix} \tag{41}$$

contains the nodal values of the pressure p. We discretise the test function ζ for the pressure also in a Bubnov-Galerkin sense:

$$\zeta = \mathbf{h}_p^{\mathrm{T}}\mathbf{z}, \tag{42}$$

with $\mathbf{z}$ the corresponding nodal array. The gradients needed in subsequent elaborations are assembled in a matrix

$$\mathbf{B}_p = \begin{pmatrix} \frac{\partial (h_p)_1}{\partial x} & ... & ... & \frac{\partial (h_p)_N}{\partial x} \\ \frac{\partial (h_p)_1}{\partial y} & ... & ... & \frac{\partial (h_p)_N}{\partial y} \\ \frac{\partial (h_p)_1}{\partial z} & ... & ... & \frac{\partial (h_p)_N}{\partial z} \end{pmatrix} \tag{43}$$

so that

$$\nabla p = \mathbf{B}_p\mathbf{p}. \tag{44}$$

When we define the external force vector $\mathbf{f}^{\mathrm{ext}}$ as in Equation (23),

$$\mathbf{f}_u^{\mathrm{ext}} = \int_{\Gamma_t} \mathbf{B}_u^{\mathrm{T}}\mathbf{t}_p \mathrm{d}\Gamma \tag{45}$$

formally the same format for the discrete equilibrium equation is obtained as in Equation (22):

$$\mathbf{f}_u^{\mathrm{ext}} - \mathbf{f}_u^{\mathrm{int}} = \mathbf{0}. \tag{46}$$

However, the interface term is now elaborated as:

$$\int_{\Gamma_d} [\![\boldsymbol{\eta}]\!] \cdot (\mathbf{t}_d^{\mathrm{loc}} - p\mathbf{n}_{\Gamma_d}^{\mathrm{loc}})\, \mathrm{d}\Gamma = \int_{\Gamma_d} \tilde{\mathbf{w}}^{\mathrm{T}}\mathbf{B}_d^{\mathrm{T}}(\mathbf{t}_d - p\mathbf{n}_{\Gamma_d})\, \mathrm{d}\Gamma, \tag{47}$$

so that the internal force vector reads:

$$\mathbf{f}_u^{\mathrm{int}} = \int_{\Omega} \mathbf{B}_u^{\mathrm{T}}(\boldsymbol{\sigma}_s - \alpha p\mathbf{m})\mathrm{d}\Omega + \int_{\Gamma_d} \mathbf{B}_d^{\mathrm{T}}(\mathbf{t}_d - p\mathbf{n}_{\Gamma_d})\, \mathrm{d}\Gamma. \tag{48}$$

with $\mathbf{m}^{\mathrm{T}} = (1, 1, 1, 0, 0, 0)$ in Voigt notation. Linearisation of the internal force vector

$\mathbf{f}_u^{\text{int}}$ then results in:

$$\mathbf{K}_{uu,j-1} = \frac{\partial \mathbf{f}_{u,j-1}^{\text{int}}}{\partial \mathbf{a}} = \underbrace{\int_\Omega \mathbf{B}_u^{\mathrm{T}} \mathbf{D}_{j-1} \mathbf{B}_u \, \mathrm{d}\Omega}_{\mathbf{K}_{uu,j-1}^{\Omega}} + \underbrace{\int_{\Gamma_d} \mathbf{B}_d^{\mathrm{T}} \mathbf{R}^{\mathrm{T}} \mathbf{D}_{d,j-1} \mathbf{R} \mathbf{B}_d \, \mathrm{d}\Gamma}_{\mathbf{K}_{uu,j-1}^{\Gamma_d}} \tag{49a}$$

$$\mathbf{K}_{up,j-1} = \frac{\partial \mathbf{f}_{u,j-1}^{\text{int}}}{\partial \mathbf{p}} = -\underbrace{\int_\Omega \alpha \mathbf{B}_u^{\mathrm{T}} \mathbf{m} \mathbf{h}_p^{\mathrm{T}} \, \mathrm{d}\Omega}_{-\mathbf{K}_{up,j-1}^{\Omega}} - \underbrace{\int_{\Gamma_d} \mathbf{B}_d^{\mathrm{T}} \mathbf{n}_{\Gamma_d} \mathbf{h}_p^{\mathrm{T}} \, \mathrm{d}\Gamma}_{-\mathbf{K}_{up,j-1}^{\Gamma_d}}. \tag{49b}$$

We next recall the weak form of the mass balance, Equation (37):

$$-\int_\Omega \alpha \zeta \nabla \cdot \dot{\mathbf{u}}_s \, \mathrm{d}\Omega - \int_\Omega k_f \nabla \zeta \cdot \nabla p \, \mathrm{d}\Omega - \int_\Omega \frac{1}{M} \zeta \dot{p} \mathrm{d}\Omega + \int_{\Gamma_d} \zeta \mathbf{n}_{\Gamma_d} \cdot [\![\mathbf{q}_d]\!] \mathrm{d}\Gamma = \int_\Gamma \zeta \mathbf{n}_\Gamma \cdot \mathbf{q}_p \mathrm{d}\Gamma.$$

Substituting the discretisations for the displacement field $\mathbf{u}_s$ and the pressure field p along with that for the corresponding test functions ζ, and requiring that the result holds for all admissible test functions, leads to the discrete format:

$$-\left(\int_\Omega \alpha \mathbf{h}_p \mathbf{m}^{\mathrm{T}} \mathbf{B}_u \mathrm{d}\Omega\right) \dot{\mathbf{a}} - \left(\int_\Omega k_f \mathbf{B}_p^{\mathrm{T}} \mathbf{B}_p \mathrm{d}\Omega\right) \mathbf{p} - \left(\int_\Omega \frac{1}{M} \mathbf{h}_p \mathbf{h}_p^{\mathrm{T}} \mathrm{d}\Omega\right) \dot{\mathbf{p}} + \underbrace{\int_{\Gamma_d} \mathbf{h}_p \mathbf{n}_{\Gamma_d}^{\mathrm{T}} [\![\mathbf{q}_d]\!] \mathrm{d}\Gamma}_{\mathbf{Q}_{\Gamma_d}} = \int_\Gamma \mathbf{h}_p \mathbf{n}_\Gamma^{\mathrm{T}} \mathbf{q}_p \mathrm{d}\Gamma. \tag{50}$$

where $\mathbf{Q}_{\Gamma_d}$ represents the rate of fluid exchange between the cavity and the bulk.

The integration over a time step Δt is commonly carried out using a Backward Euler scheme:

$$(\dot{\bullet}) = \frac{(\bullet)^{t+\Delta t} - (\bullet)^t}{\Delta t} \tag{51}$$

with the superscript denoting at which time the quantity is evaluated. Substitution of the time integration scheme into Equation (50) yields, after multiplication by Δt in order to preserve a symmetric tangential stiffness matrix:

$$\mathbf{f}_p^{\text{int}} = \mathbf{f}_p^{\text{ext}} \tag{52}$$

with the external force vector:

$$\mathbf{f}_p^{\text{ext}} = \Delta t \int_\Gamma \mathbf{h}_p \, \mathbf{n}_{\Gamma_q}^{\mathrm{T}} \mathbf{q}_p \, \mathrm{d}\Gamma \tag{53}$$

and the internal force vector:

$$\mathbf{f}_p^{\text{int}} = \underbrace{-\left(\int_\Omega \alpha \mathbf{h}_p \mathbf{m}^{\mathrm{T}} \mathbf{B}_u \mathrm{d}\Omega\right)}_{-\mathbf{K}^{\Omega}_{pu,j-1}=-\left(\mathbf{K}^{\Omega}_{up,j-1}\right)^{\mathrm{T}}} \mathbf{u}^{t+\Delta t} \underbrace{-\left(\int_\Omega \frac{1}{M} \mathbf{h}_p \mathbf{h}_p^{\mathrm{T}} \,\mathrm{d}\Omega\right)}_{-\mathbf{K}^{\Omega(1)}_{pp,j-1}} \mathbf{p}^{t+\Delta t} \underbrace{-\left(\Delta t \int_\Omega k_f \mathbf{B}_p^{\mathrm{T}} \mathbf{B}_p \,\mathrm{d}\Omega\right)}_{-\mathbf{K}^{\Omega(2)}_{pp,j-1}} \mathbf{p}^{t+\Delta t}$$
$$+ \underbrace{\left(\int_\Omega \alpha \mathbf{h}_p \mathbf{m}^{\mathrm{T}} \mathbf{B}_u \mathrm{d}\Omega\right)}_{-\mathbf{K}^{\Omega}_{pu,j-1}=\left(\mathbf{K}^{\Omega}_{up,j-1}\right)^{\mathrm{T}}} \mathbf{u}^{t} + \underbrace{\left(\int_\Omega \frac{1}{M} \mathbf{h}_p \mathbf{h}_p^{\mathrm{T}} \,\mathrm{d}\Omega\right)}_{-\mathbf{K}^{\Omega(1)}_{pp,j-1}} \mathbf{p}^{t} + \Delta t \mathbf{Q}_{\Gamma_d}. \tag{54}$$

The contributions to the tangential stiffness matrix follow in the usual manner, by differentiating $\mathbf{f}_p^{\text{int}}$ with respect to $\mathbf{a}$ and $\mathbf{p}$, respectively:

$$\frac{\partial \mathbf{f}^{\text{int}}_{p,j-1}}{\partial \mathbf{a}} = \mathbf{K}^{\Omega}_{pu,j-1} + \Delta t \frac{\partial \mathbf{Q}_{\Gamma_d}}{\partial \mathbf{a}} \tag{55a}$$

$$\frac{\partial \mathbf{f}^{\text{int}}_{p,j-1}}{\partial \mathbf{p}} = \mathbf{K}^{\Omega(1)}_{pp,j-1} + \mathbf{K}^{\Omega(2)}_{pp,j-1} + \Delta t \frac{\partial \mathbf{Q}_{\Gamma_d}}{\partial \mathbf{p}}. \tag{55b}$$

Hence, the complete linearised set of equations, needed in a Newton-Raphson framework, reads:

$$\begin{bmatrix} \mathbf{K}^{\Omega}_{uu,j-1} + \mathbf{K}^{\Gamma_d}_{uu,j-1} & \mathbf{K}^{\Omega}_{up,j-1} + \mathbf{K}^{\Gamma_d}_{up,j-1} \\ \mathbf{K}^{\Omega}_{pu,j-1} + \Delta t \left.\frac{\partial \mathbf{Q}_{\Gamma_d}}{\partial \mathbf{a}}\right|_{j-1} & \mathbf{K}^{\Omega(1)}_{pp,j-1} + \mathbf{K}^{\Omega(2)}_{pp,j-1} + \Delta t \left.\frac{\partial \mathbf{Q}_{\Gamma_d}}{\partial \mathbf{p}}\right|_{j-1} \end{bmatrix} \begin{Bmatrix} \mathrm{d}\mathbf{a} \\ \mathrm{d}\mathbf{p} \end{Bmatrix} = \begin{Bmatrix} \mathbf{f}^{\text{ext}}_u \\ \mathbf{f}^{\text{ext}}_p \end{Bmatrix} - \begin{Bmatrix} \mathbf{f}^{\text{int}}_{u,j-1} \\ \mathbf{f}^{\text{int}}_{p,j-1} \end{Bmatrix}. \tag{56}$$

It is noted that the terms $\mathbf{K}^{\Gamma_d}_{up}$ and $\Delta t \frac{\partial \mathbf{Q}_{\Gamma_d}}{\partial \mathbf{a}}$ render the tangential stiffness matrix non-symmetric, and are omitted in most computations.

To compute

$$\mathbf{Q}_{\Gamma_d} = \int_{\Gamma_d} \mathbf{h}_p \mathbf{n}^{\mathrm{T}}_{\Gamma_d} [\![\mathbf{q}_d]\!] \mathrm{d}\Gamma \tag{57}$$

we recall that the local rate of fluid exchange between an open cavity and the surrounding bulk material is given by [11, 13]:

$$\mathbf{n}^{\mathrm{T}}_{\Gamma_d} [\![\mathbf{q}_d]\!] = n_f \left(\frac{h^3}{12\mu} \frac{\partial^2 p}{\partial s^2} + \frac{h^2}{4\mu} \frac{\partial h}{\partial s} \frac{\partial p}{\partial s} - h \left(\frac{\partial (\dot{u}_s)_s}{\partial s} - \frac{k_f}{n_f} \frac{\partial^2 p}{\partial s^2} \right) - \frac{\partial h}{\partial t} \right) \tag{58}$$

where the resemblance to Reynolds lubrication equation can be noted [28], and μ is the fluid viscosity and h the width of the cavity, Figure 1. From this equation we observe that higher-order derivatives and non-standard terms have to be computed. Therefore, the matrix

$$\mathbf{B}_p^2 = \begin{pmatrix} \frac{\partial^2 (h_p)_1}{\partial x^2} & \dots & \dots & \frac{\partial (h_p)_N}{\partial x^2} \\ \frac{\partial^2 (h_p)_1}{\partial y^2} & \dots & \dots & \frac{\partial (h_p)_N}{\partial y^2} \\ \frac{\partial^2 (h_p)_1}{\partial z^2} & \dots & \dots & \frac{\partial (h_p)_N}{\partial z^2} \end{pmatrix} \tag{59}$$

is defined such that

$$\frac{\partial^2 p}{\partial s^2} = \mathbf{s}_{\Gamma_d}^{\mathrm{T}} \mathbf{B}_p^2 \mathbf{p}, \tag{60}$$

the matrix

$$\mathbf{B}_{d,s} = \begin{bmatrix} -\frac{\partial \mathbf{h}}{\partial s} & +\frac{\partial \mathbf{h}}{\partial s} & \mathbf{0} & \mathbf{0} & \mathbf{0} & \mathbf{0} \\ \mathbf{0} & \mathbf{0} & -\frac{\partial \mathbf{h}}{\partial s} & +\frac{\partial \mathbf{h}}{\partial s} & \mathbf{0} & \mathbf{0} \\ \mathbf{0} & \mathbf{0} & \mathbf{0} & \mathbf{0} & -\frac{\partial \mathbf{h}}{\partial s} & +\frac{\partial \mathbf{h}}{\partial s} \end{bmatrix}, \tag{61}$$

which is needed to compute

$$\frac{\partial h}{\partial s} = \mathbf{n}_{\Gamma_d}^{\mathrm{T}} \mathbf{B}_{d,s} \mathbf{a}, \tag{62}$$

while the tangential gradient of the solid velocity can be approximated as the average of the velocities at Γ_d^+ and Γ_d^-:

$$\frac{\partial (\dot{u}_s)_s}{\partial s} \approx \mathbf{s}_{\Gamma_d}^{\mathrm{T}} \bar{\mathbf{B}}_{d,s} \dot{\mathbf{a}}, \tag{63}$$

The operator matrix $\bar{\mathbf{B}}_{d,s}$ is built similar to $\mathbf{B}_{d,s}$, except that the coefficients ± 1 are replaced by $\frac{1}{2}$. Using these identities, we obtain

$$\begin{aligned} \mathbf{Q}_{\Gamma_d} = \int_{\Gamma_d} \mathbf{h}_p \Bigg(& \frac{n_f}{12\mu} \left(\mathbf{n}_{\Gamma_d}^{\mathrm{T}} \mathbf{B}_d \mathbf{a} \right)^3 \left(\mathbf{s}_{\Gamma_d}^{\mathrm{T}} \mathbf{B}_p^2 \mathbf{p} \right) \\ & + \frac{n_f}{4\mu} \left(\mathbf{n}_{\Gamma_d}^{\mathrm{T}} \mathbf{B}_d \mathbf{a} \right)^2 \left(\mathbf{n}_{\Gamma_d}^{\mathrm{T}} \mathbf{B}_{d,s} \mathbf{a} \right) \left(\mathbf{s}_{\Gamma_d}^{\mathrm{T}} \mathbf{B}_p \mathbf{p} \right) \\ & - \left(\mathbf{n}_{\Gamma_d}^{\mathrm{T}} \mathbf{B}_d \mathbf{a} \right) \left(\mathbf{s}_{\Gamma_d}^{\mathrm{T}} \bar{\mathbf{B}}_{d,s} \dot{\mathbf{a}} - \frac{k_f}{n_f} \mathbf{s}_{\Gamma_d}^{\mathrm{T}} \mathbf{B}_p^2 \mathbf{p} \right) - \mathbf{n}_{\Gamma_d}^{\mathrm{T}} \mathbf{B}_d \dot{\mathbf{a}} \Bigg) \mathrm{d}\Gamma. \end{aligned} \tag{64}$$

From this expression it is evident that the derivatives

$$\frac{\partial \mathbf{Q}_{\Gamma_d}}{\partial \mathbf{a}} \quad \text{and} \quad \frac{\partial \mathbf{Q}_{\Gamma_d}}{\partial \mathbf{p}} \tag{65}$$

lead to very cumbersome and lengthy expressions, which is another reason why they are normally not incorporated in the tangential stiffness matrix. Moreover, $\frac{\partial \mathbf{Q}_{\Gamma_d}}{\partial \mathbf{p}}$ adds another non-symmetry to the tangential stiffness matrix.

3.2. Interface elements with a discontinuous pressure

In case of a possible discontinuous pressure across the interface element, i.e. when there are two pressure nodes, Figure 2(b), the fluid flux in the interface reads:

$$\mathbf{n}_{\Gamma_d} \cdot [\![\mathbf{q}_d]\!] = -k_{nd} (p^+ - p^-) = -k_{nd} [\![p]\!] \tag{66}$$

The discretisation of the pressure jump is similar to that of the displacement jump, cf. Equation (6),

$$[\![\mathbf{p}]\!] = (p^+ - p^-) = (\mathbf{h}_p^{\mathrm{T}} \mathbf{p}^+ - \mathbf{h}_p^{\mathrm{T}} \mathbf{p}^-) = \mathbf{H}_p \tilde{\mathbf{p}}, \tag{67}$$

with

$$\mathbf{H}_p = \begin{bmatrix} -\mathbf{h}_p^{\mathrm{T}} & \mathbf{h}_p^{\mathrm{T}} \end{bmatrix}. \tag{68}$$

The array $\tilde{\mathbf{p}}$ contains the discrete nodal pressures at both sides of the interface. Similar to the displacements, globally no degrees of freedom are added although $\tilde{\mathbf{p}}$ contains twice the number of degrees of freedom as does $\mathbf{p}$ per element. Substitution of Equation (68) into Equation (67) then gives:

$$\mathbf{n}_{\Gamma_d} \cdot [\![\mathbf{q}_d]\!] = -k_{nd}\mathbf{H}_p\mathbf{p}. \tag{69}$$

An anomaly of the approach is that there is no (separate) pressure within the interface. As a consequence, the pressure vanishes from the stress continuity condition across the interface and, instead of Equation (48), we have for the interface contribution to the internal force vector:

$$\mathbf{f}_u^{\text{int}} = \int_\Omega \mathbf{B}_u^{\mathrm{T}}(\boldsymbol{\sigma}_s - \alpha p\mathbf{m})\mathrm{d}\Omega + \int_{\Gamma_d} \mathbf{B}_d^{\mathrm{T}}\mathbf{t}_d \, \mathrm{d}\Gamma. \tag{70}$$

Since in the absence of an explicitly defined pressure in the discontinuity, $\mathbf{f}_u^{\text{int}}$ no longer depends on it, the interface stiffness term $\mathbf{K}_{up}^{\Gamma_d}$ cancels as well, and only the interface stiffness $\mathbf{K}_{uu}^{\Gamma_d}$ remains.

The interface term in the mass balance also simplifies. Noting that, similar to the displacement discontinuity, the jump in the test function, $[\![\zeta]\!]$, is interpolated in a Bubnov-Galerkin sense as:

$$[\![\zeta]\!] = \mathbf{H}_p\tilde{\mathbf{z}}, \tag{71}$$

the interface term in the weak form of the mass balance, Equation (37), can be elaborated as:

$$\int_{\Gamma_d} [\![\zeta]\!] \, \mathbf{n}_{\Gamma_d} \cdot [\![\mathbf{q}_d]\!]\mathrm{d}\Gamma = -\tilde{\mathbf{z}}^{\mathrm{T}} \int_{\Gamma_d} k_{nd}\mathbf{H}_p^{\mathrm{T}}\mathbf{H}_p\tilde{\mathbf{p}}\mathrm{d}\Gamma \tag{72}$$

where Equation (69) has been used. Since this expression must hold for all admissible test functions for the pressure, the contribution that stems from the internal discontinuity to the internal force vector becomes, after multiplication by Δt for symmetry reasons:

$$-\Delta t\left(\int_{\Gamma_d} k_{nd}\mathbf{H}_p^{\mathrm{T}}\mathbf{H}_p\mathrm{d}\Gamma\right)\mathbf{p} \tag{73}$$

Hence, the only non-vanishing contribution from the internal discontinuity to the tangential stiffness matrix becomes:

$$\mathbf{K}_{pp}^{\Gamma_d} = -\Delta t \int_{\Gamma_d} k_{nd}\mathbf{H}_p^{\mathrm{T}}\mathbf{H}_p\mathrm{d}\Gamma. \tag{74}$$

Physically, this choice seems less reasonable, also because the absence of a (separate) pressure within the crack also precludes fluid transport along the crack. In reality some assumption for the fluid pressure in the crack must be made, a linear interpolation between p^- and p^+ being the simplest possible hypothesis. In fact, this is precisely the proposal which has been made by [25] in their enhancement of interface elements with two pressure nodes. Nevertheless, taking the fluid pressure in the crack as the average of those at the two sides of the cavity makes it impossible to model hydraulic fracturing, where the fluid pressure must be an independent variable.

3.3. An independent pressure in the interface

The deficiency of the discontinuous pressure model can be remedied by superimposing a (regularised) Dirac function for the pressure, in the spirit of the local enrichment proposed by [21]. The independent pressures are now p^- at the Γ_d^--side of the interface Γ_d, p^+ at the Γ_d^+-side and p_d within the interface. Clearly, the existence of an independent pressure within the discontinuity allows for modelling pressurising the crack, which permits extension of the modelling capabilities to hydraulic fracturing.

Different from the previous two cases, an explicit distinction must now be made between the inflow of fluid through the Γ^- and Γ^+-interfaces. In principle, the resistance at both boundaries can be different, and (time-dependent) expressions for leak-off have been derived based on a heat conduction analogy [26]. Herein, we simply assume that the resistance to flow is the same at both boundaries of the cavity, k_{nd}. Then, the following relation ensues between the flux into the discontinuity and the different fluid pressures:

$$\mathbf{n}_{\Gamma_d} \cdot [\![\mathbf{q}_d]\!] = -k_{nd}\,(p^- - p_d) - k_{nd}(p^+ - p_d) = k_{nd}(2p_d - p^+ - p^-). \tag{75}$$

The sum of the pressures p^- and p^+ is interpolated as

$$p^+ + p^- = \mathbf{H}_p \tilde{\mathbf{p}}, \tag{76}$$

with $\mathbf{H}_p$ redefined as

$$\mathbf{H}_p = \begin{bmatrix} \mathbf{h}_p^{\mathrm{T}} & \mathbf{h}_p^{\mathrm{T}} \end{bmatrix}. \tag{77}$$

Evidently, there must now be a separate interpolation for p_d:

$$p_d = \mathbf{h}_d^{\mathrm{T}} \mathbf{p}_d \tag{78}$$

where the vector

$$\mathbf{h}_d^{\mathrm{T}} = ((h_d)_1, ..., (h_d)_N) \tag{79}$$

contains the interpolation polynomials for the pressure in the discontinuity, and

$$\mathbf{p}_d = \begin{pmatrix} (p_d)_1 \\ ... \\ ... \\ (p_d)_N \end{pmatrix} \tag{80}$$

contains the nodal values of the pressure p_d. We discretise the test function ζ_d for the pressure in the discontinuity also in a Bubnov-Galerkin sense:

$$\zeta_d = \mathbf{h}_d^{\mathrm{T}} \mathbf{z}_d, \tag{81}$$

with $\mathbf{z}_d$ the corresponding nodal array. Again, gradients are needed and are assembled in a matrix:

$$\mathbf{B}_{pd} = \begin{pmatrix} \frac{\partial (h_d)_1}{\partial x} & ... & ... & \frac{\partial (h_d)_N}{\partial x} \\ \frac{\partial (h_d)_1}{\partial y} & ... & ... & \frac{\partial (h_d)_N}{\partial y} \\ \frac{\partial (h_d)_1}{\partial z} & ... & ... & \frac{\partial (h_d)_N}{\partial z} \end{pmatrix} \tag{82}$$

so that

$$\nabla p_d = \mathbf{B}_{pd}\mathbf{p}_d \tag{83}$$

Using Equations (76) and (78), Equation (75) can be rewritten as:

$$\mathbf{n}_{\Gamma_d} \cdot [\![\mathbf{q}_d]\!] = 2k_{nd}\mathbf{h}_d^{\mathrm{T}}\mathbf{p}_d - k_{nd}\mathbf{H}_p\tilde{\mathbf{p}}. \tag{84}$$

Since there is now an independent pressure p_d within the discontinuity, the internal force vector that stems from the momentum balance remains as in the single pressure model:

$$\mathbf{f}_u^{\mathrm{int}} = \int_\Omega \mathbf{B}_u^{\mathrm{T}}(\boldsymbol{\sigma}_s - \alpha p\mathbf{m})\mathrm{d}\Omega + \int_{\Gamma_d} \mathbf{B}_d^{\mathrm{T}}(\mathbf{t}_d - p_d\mathbf{n}_{\Gamma_d})\,\mathrm{d}\Gamma, \tag{85}$$

cf. Equation (48). Three separate contributions to the tangential stiffness matrix can now identified:

$$\mathbf{K}_{uu,j-1} = \frac{\partial \mathbf{f}_{u,j-1}^{\mathrm{int}}}{\partial \mathbf{a}} = \underbrace{\int_\Omega \mathbf{B}_u^{\mathrm{T}}\mathbf{D}_{j-1}\mathbf{B}_u\,\mathrm{d}\Omega}_{\mathbf{K}^{\Omega}_{uu,j-1}} + \underbrace{\int_{\Gamma_d} \mathbf{B}_d^{\mathrm{T}}\mathbf{R}^{\mathrm{T}}\mathbf{D}_{d,j-1}\mathbf{R}\mathbf{B}_d\,\mathrm{d}\Gamma}_{\mathbf{K}^{\Gamma_d}_{uu,j-1}} \tag{86a}$$

$$\mathbf{K}_{up,j-1} = \frac{\partial \mathbf{f}_{u,j-1}^{\mathrm{int}}}{\partial \mathbf{p}} = \underbrace{-\int_\Omega \alpha\mathbf{B}_u^{\mathrm{T}}\mathbf{m}\mathbf{h}_p^{\mathrm{T}}\,\mathrm{d}\Omega}_{-\mathbf{K}^{\Omega}_{up,j-1}} \tag{86b}$$

$$\mathbf{K}_{ud,j-1} = \frac{\partial \mathbf{f}_{u,j-1}^{\mathrm{int}}}{\partial \mathbf{p}_d} = \underbrace{-\int_{\Gamma_d} \mathbf{B}_d^{\mathrm{T}}\mathbf{n}_{\Gamma_d}\mathbf{h}_d^{\mathrm{T}}\,\mathrm{d}\Gamma}_{-\mathbf{K}^{\Gamma_d}_{ud,j-1}}. \tag{86c}$$

After multiplication by Δt for symmetry-preserving reasons, the contributions from the global mass balance to the tangential stiffness become:

$$\mathbf{K}_{pu,j-1} = \frac{\partial \mathbf{f}_{p,j-1}^{\mathrm{int}}}{\partial \mathbf{a}} = \underbrace{-\int_\Omega \alpha\mathbf{h}_p\mathbf{m}^{\mathrm{T}}\mathbf{B}_u}_{-\mathbf{K}^{\Omega}_{pu,j-1}} \tag{87a}$$

$$\mathbf{K}_{pp,j-1} = \frac{\partial \mathbf{f}_{p,j-1}^{\mathrm{int}}}{\partial \mathbf{p}} = \underbrace{-\int_\Omega \frac{1}{M}\mathbf{h}_p^{\mathrm{T}}\mathbf{h}_p\mathrm{d}\Omega}_{-\mathbf{K}^{\Omega(1)}_{pp,j-1}} \underbrace{-\Delta t\int_\Omega k_f\mathbf{B}_p^{\mathrm{T}}\mathbf{B}_p\mathrm{d}\Omega}_{-\mathbf{K}^{\Omega(2)}_{pp,j-1}} \underbrace{-\Delta t\int_{\Gamma_d} k_{nd}\mathbf{H}_p^{\mathrm{T}}\mathbf{H}_p\mathrm{d}\Gamma}_{-\mathbf{K}^{\Gamma_d}_{pp,j-1}} \tag{87b}$$

$$\mathbf{K}_{pd,j-1} = \frac{\partial \mathbf{f}_{p,j-1}^{\mathrm{int}}}{\partial \mathbf{p}_d} = \underbrace{2\Delta t\int_{\Gamma_d} k_{nd}\mathbf{h}_p\mathbf{h}_d^{\mathrm{T}}\mathrm{d}\Gamma}_{\mathbf{K}^{\Gamma_d}_{pd,j-1}}. \tag{87c}$$

where the weak form of Equation (84) has been exploited:

$$\int_{\Gamma_d} \zeta\mathbf{n}_{\Gamma_d} \cdot [\![\mathbf{q}_d]\!]\mathrm{d}\Gamma = \int_{\Gamma_d} 2k_{nd}\zeta\mathbf{h}_d^{\mathrm{T}}\mathbf{p}_d\mathrm{d}\Gamma - \int_{\Gamma_d} k_{nd}[\![\zeta]\!]\mathbf{H}_p\tilde{\mathbf{p}}\mathrm{d}\Gamma. \tag{88}$$

To complete the set of governing equations, the local mass balance at the discontinuity

$$2k_{nd}p_d - k_{nd}(p^- + p^+) - n_f\left(\frac{h^3}{12\mu}\frac{\partial^2 p_d}{\partial s^2} + \frac{h^2}{4\mu}\frac{\partial h}{\partial s}\frac{\partial p_d}{\partial s} - h\left(\frac{\partial(\dot{u}_s)_s}{\partial s} - \frac{k_f}{n_f}\frac{\partial^2 p_d}{\partial s^2}\right) - \frac{\partial h}{\partial t}\right) = 0, \tag{89}$$

which is obtained by combining Equations (58) and (75), is cast in a weak format. After multiplication by the test function ζ_d, integration over Γ_d, and application of Gauss' theorem, the following identity results:

$$\begin{aligned}\int_{\Gamma_d}\Bigg(&2k_{nd}\zeta_d p_d - k_{nd}\zeta_d(p^- + p^+) + \left(\frac{n_f h^3}{12\mu} + k_f h\right)\frac{\partial\zeta_d}{\partial s}\frac{\partial p_d}{\partial s}\\ &- n_f\zeta_d\left(\frac{h^2}{4\mu}\frac{\partial h}{\partial s}\frac{\partial p_d}{\partial s} - h\frac{\partial(\dot{u}_s)_s}{\partial s} - \frac{\partial h}{\partial t}\right)\Bigg)\mathrm{d}\Gamma = Q_{\mathrm{tip}},\end{aligned} \tag{90}$$

where Q_{tip} is the inflow of fluid at the crack tip. Multiplication by Δt and discretisation then leads to:

$$\mathbf{K}_{du}^{\Gamma_d}\mathbf{a} + \mathbf{K}_{dp}^{\Gamma_d}\mathbf{p} + \mathbf{K}_{dd}^{\Gamma_d}\mathbf{p}_d = \mathbf{f}_{p_d}^{\mathrm{ext}}, \tag{91}$$

with the submatrices $\mathbf{K}_{du}^{\Gamma_d}$, $\mathbf{K}_{dp}^{\Gamma_d}$, $\mathbf{K}_{dd}^{\Gamma_d}$ defined as:

$$\mathbf{K}_{du}^{\Gamma_d} = \int \Gamma_d\left(n_f h\mathbf{s}_{\Gamma_d}^{\mathrm{T}}\bar{\mathbf{B}}_{d,s} + n_f\mathbf{n}_{\Gamma_d}^{\mathrm{T}}\mathbf{B}_d\right)\mathrm{d}\Gamma \tag{92a}$$

$$\mathbf{K}_{dp}^{\Gamma_d} = -\Delta t\int_{\Gamma_d} k_{nd}\mathbf{h}_d\mathbf{H}_p\mathrm{d}\Gamma \tag{92b}$$

$$\mathbf{K}_{dd}^{\Gamma_d} = \Delta t\int_{\Gamma_d}\left(2k_{nd}\mathbf{h}_d\mathbf{h}_d^{\mathrm{T}} + \left(\frac{n_f h^3}{12\mu} + k_f h\right)\mathbf{B}_{pd}^{\mathrm{T}}\mathbf{s}_{\Gamma_d}\mathbf{s}_{\Gamma_d}^{\mathrm{T}}\mathbf{B}_{pd} - \frac{n_f h^2}{4\mu}\frac{\partial h}{\partial s}\mathbf{h}_d\mathbf{s}_{\Gamma_d}^{\mathrm{T}}\mathbf{B}_{pd}\right)\mathrm{d}\Gamma. \tag{92c}$$

As for the case of a single pressure node, we have:

$$h^n = \left(\mathbf{n}_{\Gamma_d}^{\mathrm{T}}\mathbf{B}_d\mathbf{a}\right)^n \quad , \quad n = 1, 2, 3 \tag{93a}$$

$$\frac{\partial h}{\partial s} = \mathbf{n}_{\Gamma_d}^{\mathrm{T}}\mathbf{B}_{d,s}\mathbf{a} \tag{93b}$$

cf. Equation (64). The linearised set of equations now reads:

$$\begin{aligned}&\begin{bmatrix}\mathbf{K}_{uu,j-1}^{\Omega} + \mathbf{K}_{uu,j-1}^{\Gamma_d} & \mathbf{K}_{up,j-1}^{\Omega} & \mathbf{K}_{ud,j-1}^{\Gamma_d}\\ \mathbf{K}_{pu,j-1}^{\Omega} & \mathbf{K}_{pp,j-1}^{\Omega(1)} + \mathbf{K}_{pp,j-1}^{\Omega(2)} + \mathbf{K}_{pp,j-1}^{\Gamma_d} & \mathbf{K}_{pd,j-1}^{\Gamma_d}\\ \mathbf{K}_{du,j-1}^{\Gamma_d} & \mathbf{K}_{dp,j-1}^{\Gamma_d} & \mathbf{K}_{dd,j-1}^{\Gamma_d}\end{bmatrix}\begin{pmatrix}\mathrm{d}\mathbf{a}\\ \mathrm{d}\mathbf{p}\\ \mathrm{d}\mathbf{p}_d\end{pmatrix}\\ &\qquad = \begin{pmatrix}\mathbf{f}_u^{\mathrm{ext}}\\ \mathbf{f}_p^{\mathrm{ext}}\\ \mathbf{f}_{p_d}^{\mathrm{ext}}\end{pmatrix} - \begin{pmatrix}\mathbf{f}_{u,j-1}^{\mathrm{int}}\\ \mathbf{f}_{p,j-1}^{\mathrm{int}}\\ \mathbf{0}\end{pmatrix}.\end{aligned} \tag{94}$$

Similar to the case with a single pressure node, the terms at the internal discontinuity render the tangential stiffness matrix non-symmetric, and are normally not included in computations.

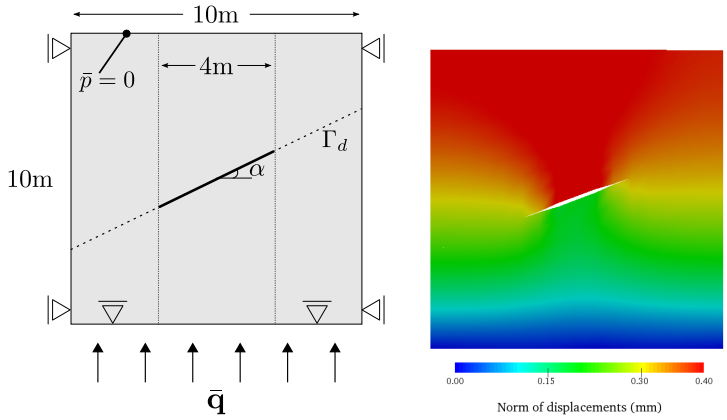

Figure 4: Square plate crossed by an interface with an inclined crack: (a) geometry, and (b) contour plot of displacements at steady state

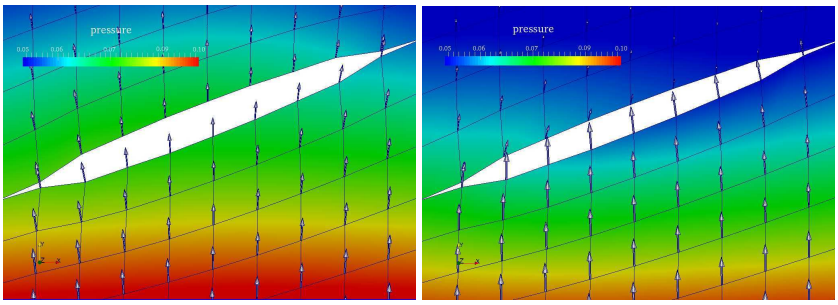

Figure 5: Pressure contour and flux vectors in the vicinity of the opened cavity at t=1s. Left: without flow in the cavity. Right: with flow in the cavity

4. Examples

4.1. Continuous pressure at the interface

As a first example, the square block of Figure 4 is considered. It is crossed by a discontinuity inclined at an angle α. The central part of Γ_d is traction free, and a model with a single pressure degree of freedom at the interface is considered. A quasi-incompressible, viscous fluid is considered with $M = 10^{18}$ MPa. The Young's modulus is taken as $E = 9.10^3$ MPa and Poisson's ratio is assumed as $\nu = 0.4$. The dummy stiffnesses at the interface are chosen as $d_n = d_s = 10^5$ MPa. The permeability is taken as $k_f = 10^3$ mm^{4}N^{-1}s^{-1}, the fluid viscosity $\mu = 10^{-9}$ Nmm^{-2}s^{-1}, and the

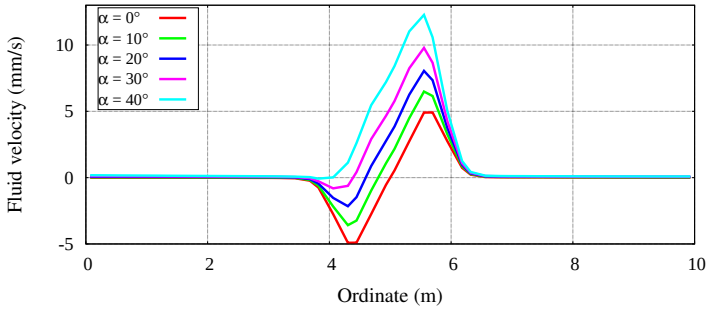

Figure 6: Tangential fluid velocity along the interface at steady state

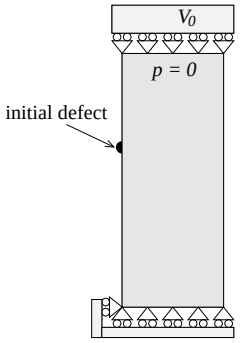

Figure 7: Geometry and boundary conditions of two–dimensional example problem

porosity $n_f = 0.3$. Non-Uniform Rational B-Splines have been used for the spatial discretisation, with the displacements interpolated by cubic splines and the pressure interpolated by quadratic splines [23]. Matching interface elements have been used to model the (stationary) discontinuity.

Figure 5 shows the effects of the flow in the cavity on the area surrounding the cavity at an early stage of the simulation. When the term for the flow in the discontinuity is made inactive, the flux is the same at both faces of the discontinuity, i.e. the fluid flows through the cavity without being affected by it. The jump in the fluid flow is clear in the right part of Figure 5, with fluid being stored and flowing away within the cavity.

Figure 6 shows that for a horizontal crack ($\alpha = 0$), the fluid velocity is symmetric in the cavity, flowing to the left and to the right in equal amounts. When the interface is inclined, the fluid can accelerate in the cavity, which starts to behave like a resistance-free channel for the fluid.

4.2. Discontinuous pressure at the interface

We next consider a two-dimensional specimen having a width $w = 0.04$ m and a height $H = 0.1$ m, Figure 7, which is loaded under plane–strain conditions. The sides are traction free and the external loading is applied via an imposed constant velocity

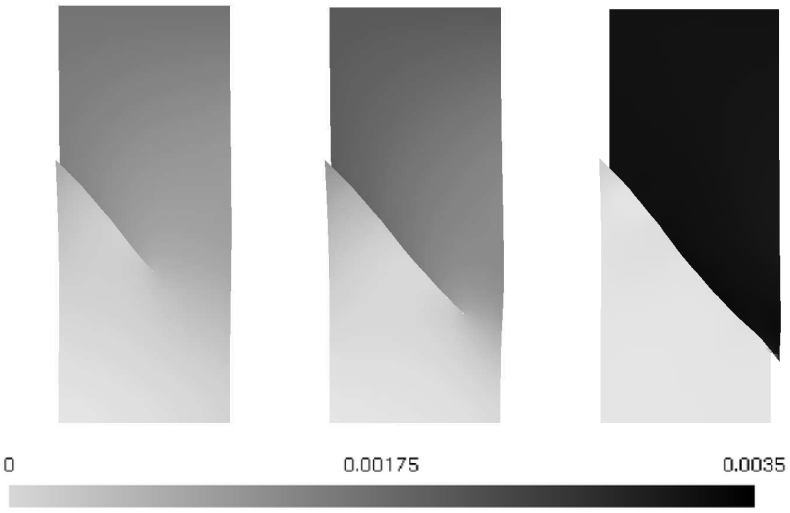

Figure 8: Evolution of the displacement field at t = 18 s, 22 s, 26 s

$V_0 = -10^{-4}$ m/s. The pore pressure at the top of the specimen is the reference pressure, here zero, and undrained boundary conditions have been imposed on the other boundaries. The solid constituent is assumed to behave in a linear elastic manner with a Young's modulus $E = 20$ GPa and a Poisson's ratio $\nu = 0.35$. The Biot coefficient α has been set equal to 1, the Biot modulus has been assigned a value $M = 5.0$ GPa, while the bulk material was assumed to have a permeability $k_f = 10^{-14}$ m^3/Ns. Shear-band formation was triggered by a small imperfection, see Figure 7. The critical shear stress at which nucleation occurred, was taken as $\tau_c = 100$ MPa and after inception the shear-band evolution is controlled by a mode-II fracture energy, $\mathcal{G}_c^{II} = 500$ J/m^2. In the example calculations, the permeability of the diaphragm has been assigned $k_{nd} = 0.5 \cdot 10^{-14}$ m^3/Ns, which is half of that in the bulk.

Different from the previous example, the specimen has been discretised with quadrilateral basis elements with a bilinear Lagrange interpolation scheme for the displacements as well as for the pressure. This scheme is not optimal, but has been used to avoid complexities in the Extended Finite Element approach that has been adopted to model the propagating shear band, especially with respect to the integration of the different parts of the load vectors and stiffness matrices in elements which are crossed by the discontinuity [10]. In the simulations, 24 elements have been used across the width of the specimen and 60 elements over the height. The simulation has been carried out in 65 equal time steps over a total time of 26 s.

Figures 8 and 9 show the evolution of the displacement field and the pressure field, respectively. At the end of the simulation, the discontinuity has traversed the entire specimen. At this point, the bulk has unloaded elastically and the external loading is transmitted entirely through the discontinuity, at which the deformations have localised. The global inclination of the interface is approximately 45^o, which is in conformity with the behaviour in a single phase medium.

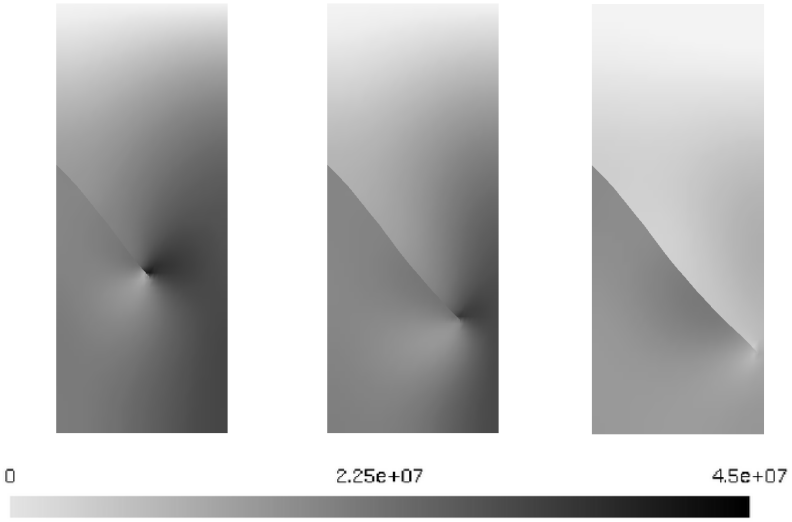

Figure 9: Evolution of the pressure field at t = 18 s, 22 s, 26 s

The pressure distribution is strongly influenced by the propagation of the interface even in the present case where k_f and k_{nd} are of the same order of magnitude. Indeed, the pressure discontinuity is significant as observed in Figure 9. Accordingly, the relatively lower permeability at the discontinuity has a major influence on the fluid flow, and therefore on the stress distribution inside the specimen.

5. Concluding remarks

A classification has been made of hydromechanical interfaces in fluid-saturated porous media. Distinction is made between one, two, and three pressure degrees of freedom. In all cases, there is a discontinuity of the pressure gradient, enabling exchange of fluid between the discontinuity and the surrounding porous bulk material. The fluid is assumed to be viscous and Newtonian, and after dimensional reduction in the direction normal to the interface, a Reynolds type equation results that governs the flow and storage within the interface. When two pressure degrees of freedom are used, a discontinuity in the pressure can be modelled at the interface, with a separate fluid resistance, but the absence of a separate, independent fluid pressure in the interface then prevents the use of a Reynolds type equation to govern possible fluid flow along the interface. This can be remedied by introducing a fluid pressure which is the average of the fluid pressures at the sides of the cavity [25], but a better solution is to rigorously introduce an independent fluid pressure, leading to a triple-node fluid pressure model [26].

Acknowledgement

Financial support through the ERC Advanced Grant 664734 ”PoroFrac” is gratefully acknowledged.

References

[1] J. G. Rots, Smeared and discrete representations of localized fracture, *International Journal of Fracture*, 51, 1991, 45–59.

[2] J. C. J. Schellekens and R. de Borst, On the numerical integration of interface elements, *International Journal for Numerical Methods in Engineering*, 36, 1993, 43–66.

[3] A. R. Ingraffea and V. Saouma, Numerical modelling of discrete crack propagation in reinforced and plain concrete. In: *Fracture Mechanics of Concrete*, Martinus Nijhoff Publishers, Dordrecht, 1985, 171–225.

[4] G. T. Camacho and M. Ortiz, Computational modelling of impact damage in brittle materials, *International Journal of Solids and Structures*, 33, 1996, 2899–2938.

[5] B. A. Schrefler, S. Secchi and L. Simoni, On adaptive refinement techniques in multifield problems including cohesive fracture, *Computer Methods in Applied Mechanics and Engineering*, 195, 2006, 444–461.

[6] S. Secchi, L. Simoni and B. A. Schrefler, Mesh adaptation and transfer schemes for discrete fracture propagation in porous materials, *International Journal for Numerical and Analytical Methods in Geomechanics*, 31, 2007, 331–345.

[7] S. Secchi, B. A. Schrefler, A method for 3-D hydraulic fracturing simulation, *International Journal of Fracture* 178, 2012, 245–258.

[8] T. Belytschko and T. Black, Elastic crack growth in finite elements with minimal remeshing, *International Journal for Numerical Methods in Engineering*, 45 (1999) 601–620.

[9] N. Moës, J. Dolbow and T. Belytschko, A finite element method for crack growth without remeshing, *International Journal for Numerical Methods in Engineering*, 46 (1999) 131–150.

[10] R. de Borst, J. Réthoré and M.A. Abellan, A numerical approach for arbitrary cracks in a fluid-saturated porous medium, *Archive of Applied Mechanics*, 75, 2006, 595–606.

[11] J. Réthoré, R. de Borst and M.-A. Abellan, A two-scale approach for fluid flow in fractured porous media, *International Journal for Numerical Methods in Engineering*, 75, 2007, 780–800.

[12] J. Réthoré, R. de Borst and M.A. Abellan, A discrete model for the dynamic propagation of shear bands in a fluid-saturated medium, *International Journal for Numerical and Analytical Methods in Geomechanics* 31, 2007, 347–370.

[13] J. Réthoré, R. de Borst and M.A. Abellan, A two-scale model for fluid flow in an unsaturated porous medium with cohesive cracks, *Computational Mechanics*, 42, 2008, 227–238.

[14] F. Irzal, J. J. C. Remmers, J. M. Huyghe and R. de Borst, A large deformation formulation for fluid flow in a progressively fracturing porous material, *Computer Methods in Applied Mechanics and Engineering*, 256, 2013, 29–37.

[15] T. Mohammadnejad and A.R. Khoei, Hydro-mechanical modelling of cohesive crack propagation in multiphase porous media using the extended finite element method, *International Journal for Numerical and Analytical Methods in Geomechanics*, 37, 2013, 1247–1279.

[16] T. Mohammadnejad and A.R. Khoei, An extended finite element method for fluid flow in partially saturated porous media with weak discontinuities: the convergence analysis of local enrichment strategies, *Computational Mechanics*, 51, 2013, 327–345.

[17] B. Carrier and S. Granet, Numerical modelling of hydraulic fracture problem in permeable medium using cohesive zone model, *Engineering Fracture Mechanics*, 79, 2012, 312–328.

[18] F. Armero and C. Callari, An analysis of strong discontinuities in a saturated poro-plastic solid, *International Journal for Numerical Methods in Engineering*, 46, 1999, 1673–1698.

[19] J. M. Segura and I. Carol, Coupled HM analysis using zero-thickness interface elements with double nodes. Part I: Theoretical model, *International Journal for Numerical and Analytical Methods in Geomechanics*, 32, 2008, 2083–2101.

[20] J. M. Segura and I. Carol, Coupled HM analysis using zero-thickness interface elements with double nodes. Part II: Verification and application, *International Journal for Numerical and Analytical Methods in Geomechanics*, 32, 2008, 2103–2123.

[21] J. Larsson and R. Larsson, Localization analysis of a fluid-saturated elastoplastic porous medium using regularized discontinuities, *Mechanics of Cohesive-frictional Materials*, 5, 2000, 565–582.

[22] F. Irzal, J. J. C. Remmers, C. V. Verhoosel and R. de Borst, An isogeometric analysis Bézier interface element for mechanical and poromechanical fracture problems, *International Journal for Numerical Methods in Engineering*, 97, 2014, 608–628.

[23] J. Vignollet, S. May and R. de Borst, Isogeometric analysis of fluid-saturated porous media including flow in the cracks, *International Journal for Numerical Methods in Engineering*, 2016, DOI: 10.1002/nme.5242.

[24] R. de Borst, M. A. Crisfield, J. J. C. Remmers and C. V. Verhoosel, *Non-Linear Finite Element Analysis of Solids and Structures*, Second Edition, Wiley & Sons, Chichester, 2012.

[25] J. M. Segura and I. Carol, On zero-thickness interface elements for diffusion problems, *International Journal for Numerical and Analytical Methods in Geomechanics*, 28, 2004, 947–962.

[26] E. W. Remij, J. J. C. Remmers, J. M. Huyghe and D. M. J. Smeulders, The enhanced local pressure model for the accurate analysis of fluid driven fracture in porous materials, *Computer Methods in Applied Mechanics and Engineering*, 286, 2015, 293–312.

[27] R. W. Lewis and B. A. Schrefler, *The Finite Element Method in the Static and Dynamic Deformation and Consolidation of Porous Media*, Second Edition, Wiley & Sons, Chichester, 1998.

[28] O. Reynolds, On the theory of lubrication and its application to Mr. Beauchamp tower's experiments, including an experimental determination of the viscosity of olive oil, *Philosophical Transactions of the Royal Society of London*, 40, 1886, 191–203.